ACS Chemical Neuroscience
Cite This: ACS Chem. Neurosci. 2018, 9, 3128−3136
Research Article
pubs.acs.org/chemneuro

In Vivo Near-Infrared Two-Photon Imaging of Amyloid Plaques in Deep Brain of Alzheimer's Disease Mouse Model

Congping Chen,[†,‡] Zhuoyi Liang,[§] Biao Zhou,[§] Xuesong Li,[†,‡] Caleb Lui,[§] Nancy Y. Ip,[*,§] and Jianan Y. Qu[*,†,‡]

[†]Biophotonics Research Laboratory, Department of Electronic and Computer Engineering, Hong Kong University of Science and Technology, Clear Water Bay, Kowloon, Hong Kong, P. R. China

[‡]Center of Systems Biology and Human Health, School of Science and Institute for Advanced Study, Hong Kong University of Science and Technology, Clear Water Bay, Kowloon, Hong Kong, P. R. China

[§]Division of Life Science and State Key Laboratory of Molecular Neuroscience, Hong Kong University of Science and Technology, Clear Water Bay, Kowloon, Hong Kong, P. R. China

ABSTRACT: Abnormal deposition of brain amyloid is a major hallmark of Alzheimer's disease (AD). The toxic extracellular amyloid plaques originating from the aberrant aggregation of beta-amyloid (Aβ) protein are considered to be the major cause of clinical deficits such as memory loss and cognitive impairment. Two-photon excited fluorescence (TPEF) microscopy provides high spatial resolution, minimal invasiveness, and long-term monitoring capability. TPEF imaging of amyloid plaques in AD transgenic mice models has greatly facilitated studies of the AD pathological mechanism. However, the imaging of deep cortical layers is still hampered by the conventional amyloid probes with short excitation/emission wavelength. In this work, we report that a near-infrared (NIR) probe, named CRANAD-3, is far superior for deep in vivo TPEF imaging of brain amyloid in comparison with the commonly used short-wavelength probe. Our findings show that the major interference for TPEF signal of the NIR probe is from the autofluorescence of lipofuscin, the "aging-pigment" in the brain. To eliminate the interference, we characterized the lipofuscin fluorescence in the aged brains of AD mice and found that it has unique broad emission and short lifetime. The lipofuscin signal can be clearly separated from the fluorescence of CRANAD-3 and fluorescent protein via a ratio-based unmixing method. Our results demonstrate the great advantages of NIR probes for in vivo deep-tissue imaging of amyloid plaques in AD.

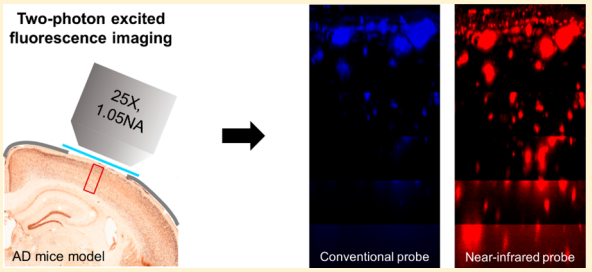

KEYWORDS: *Alzheimer's disease, amyloid plaque, multiphoton microscopy, deep brain imaging, near-infrared fluorescence probe, lipofuscin*

INTRODUCTION

Alzheimer's disease (AD) is the most common neurodegenerative disorder and the leading cause of dementia in the elderly. This currently incurable disease imposes an enormous economic burden on the society and its prevalence is rapidly increasing due to the aging population globally.[1] The pathological hallmarks of AD include the intracellular neurofibrillary tangles and extracellular amyloid plaques.[2,3] Neurofibrillary tangles are mainly composed of a misfolded microtubule-associated protein known as tau protein, while amyloid plaques are deposits and aggregates of amyloid-beta (Aβ) peptides resulting from proteolytic cleavages of the membrane-bound amyloid precursor protein (APP). Since the discovery of these significant biomarkers for AD, several hypotheses have been proposed to explain the pathogenesis of this multifactorial disease,[4−9] such as cholinergic hypothesis,[5] tau hypothesis,[8] and amyloid cascade hypothesis,[6,9] among which the amyloid cascade hypothesis has dominating influence on both academic and clinical research over the past few decades. This hypothesis suggests that the Aβ peptide produced by β- and γ-secretase is initiated by the mutations of several genes (APP, PS1 and PS2), and will spontaneously aggregate into soluble oligomer and eventually accumulate to form insoluble amyloid plaques. The neurotoxic Aβ proteins are considered to be the causative agents that will lead to progressive synaptic dysfunction and neuronal degeneration, and finally result in symptoms of Alzheimer's dementia such as memory decline and cognitive deficit.[10] Therefore, in vivo imaging of amyloid deposition in brain is of great significance for elucidating the underlying mechanism of AD pathogenesis.

The past few decades have witnessed the development of several powerful imaging techniques that offer the opportunity for noninvasive or minimally invasive detection of amyloid deposits in the intact brain, such as positron emission

Received: June 23, 2018
Accepted: August 1, 2018
Published: August 1, 2018

DOI: 10.1021/acschemneuro.8b00306
ACS Chem. Neurosci. 2018, 9, 3128−3136

tomography (PET),[11,12] single photon emission computed tomography (SPECT),[13,14] magnetic resonance imaging (MRI),[15,16] near-infrared fluorescence (NIRF) imaging,[17,18] vibrational spectroscopy,[19,20] and two-photon excitation microscopy (TPEM).[21,22] MRI, PET, and SPECT are useful tools for clinical diagnosis but not suitable for microscopic imaging of the pathological changes in the brain because of their limited spatial resolution and long acquisition time. NIRF imaging allows noninvasive detection of Aβ species with fast acquisition speed but still suffers from the poor spatial resolution and unable to resolve individual plaque. Although it has been demonstrated that vibrational spectroscopy could be potentially for clinical AD diagnosis,[23] the technology provides limited detection sensitivity and imaging resolution. On the other hand, TPEM is a form of laser-scanning microscopy based on localized nonlinear excitation that could provide both high spatial and temporal resolution.[24,25] More importantly, by using a chronic open- or thinned-skull window together with different fluorescent labels, TPEM enables long-term repetitive visualization of individual amyloid plaques and their surrounding structures inside the mouse brain.[26−28] These unique advantages make TPEM an ideal imaging tool for preclinical studies in AD mice models.

MeO-X04 is a well-known amyloid-binding probe that has been widely used for in vivo two-photon excited fluorescence (TPEF) imaging of brain amyloid because of its high specificity for amyloid deposits and good permeability of the blood-brain barrier (BBB).[21,27−30] However, due to the high scattering and absorption of biological tissue in the short wavelength range, its applications in two-photon microscopy are largely restricted to the superficial brain region, normally no more than 400 μm in depth. Two-photon imaging of amyloid plaques in deep cortical layers or subcortical regions in vivo remains a challenge. One simple and effective strategy for increasing the imaging depth of TPEM is using probes with red-shifted excitation and emission to reduce the absorption and scattering from brain tissue.[25,31] Over the past decade, there have been significant advances in the design and synthesis of NIR fluorescent probes for detection of amyloid plaques in vivo. They have great fluorescence properties such as a large Stokes shift and intensity increment upon binding to Aβ protein.[32,33] However, almost all these probes were designed and have been employed for macroscopic NIRF imaging under single-photon excitation, yielding a low spatial resolution of 1−3 mm.[29] Their performances in TPEF imaging remain largely unexplored.

In addition, it is normally inevitable to encounter the so-called "aging-pigment" lipofuscin in fluorescent imaging of aged brain. Lipofuscins are punctate-like cellular wastes that are thought to be the product of incomplete lysosomal degradation of damaged mitochondria.[34,35] They cannot be further degraded or ejected from the cell, and thus, they will accumulate in the cell with increasing age. Their heterogeneous distribution in aged brain tissue complicates fluorescent imaging in AD mice due to their strong autofluorescence emission.[36−38] Since lipofuscin interference can arise for two-photon fluorescence imaging using NIR probes or fluorescent proteins, it is necessary to discriminate the desired fluorescence signal from lipofuscin autofluorescence. Currently, the fluorescence characteristics of lipofuscin in live mice brains are poorly understood, and effective strategies for removing the lipofuscin interference for in vivo brain imaging have yet to be established.

In this work, we study a new NIR probe namely CRANAD-3 for in vivo deep two-photon imaging of brain amyloid in an AD transgenic mice model. First, the TPEF properties of CRANAD-3 and lipofuscin are individually characterized in vivo by using a spectroscopic imaging method. The TPEF properties of commonly used MeO-X04 are also characterized for the comparison study. Based on the distinct TPEF properties of NIR probe and lipofuscin, we propose a ratio-based spectral and lifetime unmixing strategy for removal of the interference signals from lipofuscin autofluorescence. Next, TPEF imaging of CRANAD-3 and MeO-X04 are compared in live mice brains through an open-skull window. The experimental results demonstrate that compared with MeO-X04, CRANAD-3 has a much larger signal-to-background ratio (SBR) in deep cortical layers. Finally, we investigate the brain immune responses to the CARNAD-3 probe. Specifically, the microglial responses to CRANAD-3 injection are studied by using TPEF imaging through a minimally invasive imaging window of thinned-skull preparation. Overall, this work aims to reveal the advantages of the NIR probe CRANAD-3 for two-photon in vivo deep-tissue imaging of amyloid plaques in AD mouse brain.

RESULTS AND DISCUSSION

In Vivo Characterization of TPEF Signals from Lipofuscin and Probes. Lipofuscin is prevalently distributed throughout the aged brain in a highly nonuniform manner. Its strong autofluorescence may cause interference in fluorescence imaging of AD brain. Therefore, the TPEF characteristics of lipofuscin are essential for differentiation of its interference from other desired TPEF signals. However, the current spectroscopic studies of lipofuscin are normally based on fixed brain samples, and their excitation spectrum and lifetime characteristics are still unclear especially in the case of living animals.[37] In this study, we first used our spectroscopic imaging system to systemically characterize the lipofuscin autofluorescence in the aged brain of APP/PS1 mice in vivo through open-skull windows (see details in Methods). As shown in the lipofuscin (top) row of Figure 1, the TPEF signals of lipofuscin exhibit unique spectral and temporal

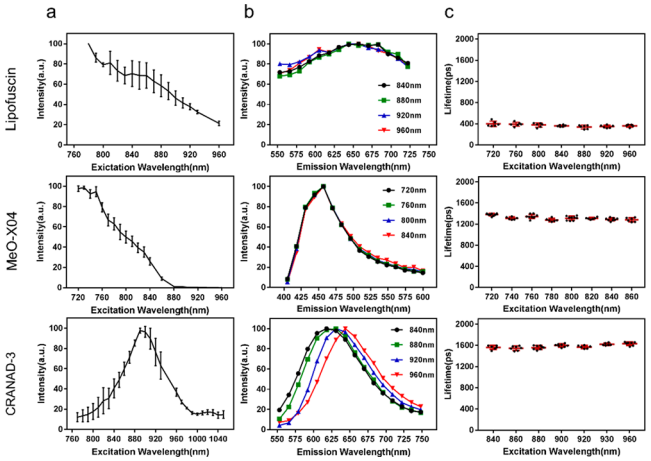

Figure 1. In vivo spectral and temporal properties of lipofuscin (upper row), MeO-X04 (middle row), and CRANAD-3 (bottom row) fluorescence in the APP/PS1 mice. (a) Two-photon excitation spectra. (b) Emission spectra. (c) Lifetimes at different excitation wavelengths. Scale bar: 20 μm.

DOI: 10.1021/acschemneuro.8b00306
ACS Chem. Neurosci. 2018, 9, 3128−3136

characteristics. The excitation efficiency of lipofuscin slowly decreases from 770 to 960 nm, indicating that its autofluorescence signal can be attenuated by using longer excitation wavelength. The fluorescence emission is roughly peaked around 650 nm and has a considerably broad emission spectral bandwidth over 200 nm in terms of full width at half-maximum (fwhm). Therefore, lipofuscin signal will seriously interfere with nearly all detection channels covering from visible to NIR regions. However, the lipofuscin signals may be identified and removed by using a ratio-based spectral unmixing method because of its unique and excessively broad bandwidth. In addition, we found that the lifetime of lipofuscin fluorescence is about 0.4 ns, much shorter than most conventional fluorescent proteins and dyes,[39,40] which makes it promising to be differentiated by using a method based on fluorescence decay analysis.

Though the characterization of MeO-X04 and CRANAD-3 fluorescence were previously conducted in solution or fixed tissue samples,[41,42] their TPEF properties in living brain tissue remain poorly investigated. In this study, we used the same spectroscopic imaging system to characterize the TPEF signals measured from the amyloid plaques in the brain of live APP/PS1 mice with the injections of MeO-X04 and CRANAD-3, respectively. As can be seen in the MeO-X04 (middle) row of Figure 1, the excitation efficiency drops quickly with the increase of excitation wavelength while the fluorescence emission peak and lifetime remain about 460 nm and 1.3 ns, respectively. The panels in the CRANAD-3 (bottom) row of the Figure 1 display the TPEF properties of CRANAD-3. As can be seen, the peak excitation wavelength of CRANAD-3 is about 900 nm, while MeO-X04 has the best excitation efficiency at a shorter wavelength region of 720−750 nm (Figure 1a, middle and bottom panels). The TPEF emission of MeO-X04 always has a stable emission peak at 460 nm under different excitation wavelengths, whereas CRANAD-3 exhibits slightly red-shifted spectra with emission peak from 620 to 650 nm when using longer excitation wavelength. The results indicate that CRANAD-3 is a potentially more appropriate probe for two-photon deep brain imaging of amyloid plaques than MeO-X04 because of much longer excitation and emission wavelengths. Finally, the data in the bottom row of Figure 1c demonstrates that CRANAD-3 has a typical fluorescence lifetime of about 1.6 ns.

Spectral and Lifetime Unmixing. We developed a simple ratio-based unmixing method to identify and remove lipofuscin interference from CRANAD-3 image. This method utilizes the distinct fluorescence characteristics of these two fluorophores and can be implemented in both spectral and lifetime domains. For spectral unmixing, the TPEF images were taken from two spectral channels with and without the plaque-labeling dye signals simultaneously. The division ratio of fluorescence signals recorded in two separate channels (620 ± 30 nm for "peak" and 550 ± 25 nm for "tail" as shown in Figure 2a) was calculated by pixel-to-pixel of two images. The pixels of high and low "peak/tail" ratio are displayed in red and green, respectively, as shown in the spectral unmixing image of Figure 2b. For lifetime unmixing, the raw CRANAD-3 image of the 620 ± 30 nm wavelength band was captured in a time-resolved manner with 256 temporal channels. Instead of measuring the lifetime of signal in each pixel, we calculated the ratio of the peak and tail regions shown in Figure 2c to differentiate the short-lifetime lipofuscin and long-lifetime CRANAD-3. The pixels of high and low "peak/tail" ratio are displayed in green and red, respectively, opposite to the color coding in spectral unmixing. Figure 2b and d shows that both spectral and lifetime unmixing produced identical results after lipofuscin identification and removal, indicating that both unmixing strategies are effective. In the following study, we used a two-channel spectral unmixing method to identify and exclude the lipofuscin interference because its implementation is relatively simple especially for multicolor imaging applications.

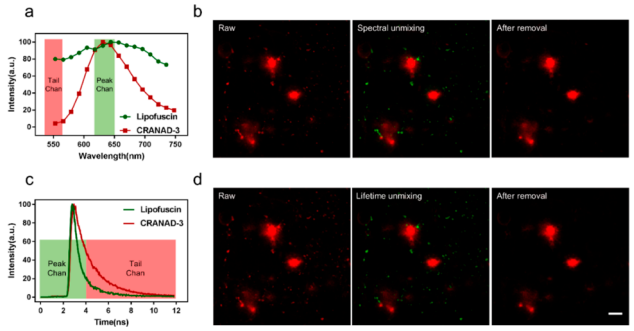

Figure 2. Ratio-based spectral and lifetime unmixing method. (a) Emission spectra of lipofuscin and CRANAD-3 at 920 nm excitation. (b) Spectral unmixing. (c) Typical lifetime curve of lipofuscin and CRANAD-3. (d) Lifetime unmixing. Scale bar: 20 μm.

In Vivo Imaging of Amyloid Plaques. To compare in vivo imaging of amyloid plaques with CRANAD-3 and MeO-X04 in APP/PS1 mice, we coinjected CRANAD-3 and MeO-X04 into the mice with dosages and delivery routes following individual protocols. In vivo TPEF imaging were conducted through the well-established open-skull window. Two detection channels (MeO-X04:447 ± 30 nm, CRANAD-3:620 ± 30 nm) were used to record their fluorescence signals and no crosstalk was observed due to their distinct emission spectra. Both of the CRANAD-3 and MeO-X04-labeled amyloid plaques in a small volume of the cortex were imaged at their optimal excitation wavelengths of 900 and 760 nm, respectively. Laser power was increased accordingly when the signal dropped significantly with increase of imaging depth, but maintained at equal for both excitation wavelengths at the same imaging depth. The maximum laser power was kept below 120 mW at the front aperture of the objective to prevent photodamage to the mice brain.

The reconstructed images of the amyloid plaques are presented in Figure 3a. The average intensity of CRANAD-3 is weaker than MeO-X04 for a 0−100 μm imaging depth below the pia, presumably because CRANAD-3, as one of curcumin analogues, has relatively smaller two-photon action cross section resulting from its relatively lower quantum yield.[43] Figure 3b shows that CRANAD-3 labeled plaques are well colocalized with those labeled by the conventional probe MeO-X04, which is consistent with previous *ex vivo* study.[44] In addition, it is noticeable that CRANAD-3 provides better labeling efficiency for the dense-core amyloid plaque than MeO-X04. With imaging depth increases beyond 200 μm, MeO-X04 intensity attenuates quickly while CRANAD-3 signal was less susceptible to imaging depth. As can be seen, the image contrast of CRANAD-3 surpassed MeO-X04 significantly at deep cortical layers especially in the depth beyond 500 μm, which is attributed to the reduced tissue absorption and scattering in NIR window (650 nm−950 nm).[45] As shown in Figure 3c, although the MeO-X04 image has been overwhelmed by the background that originates from

DOI: 10.1021/acschemneuro.8b00306
ACS Chem. Neurosci. 2018, 9, 3128−3136

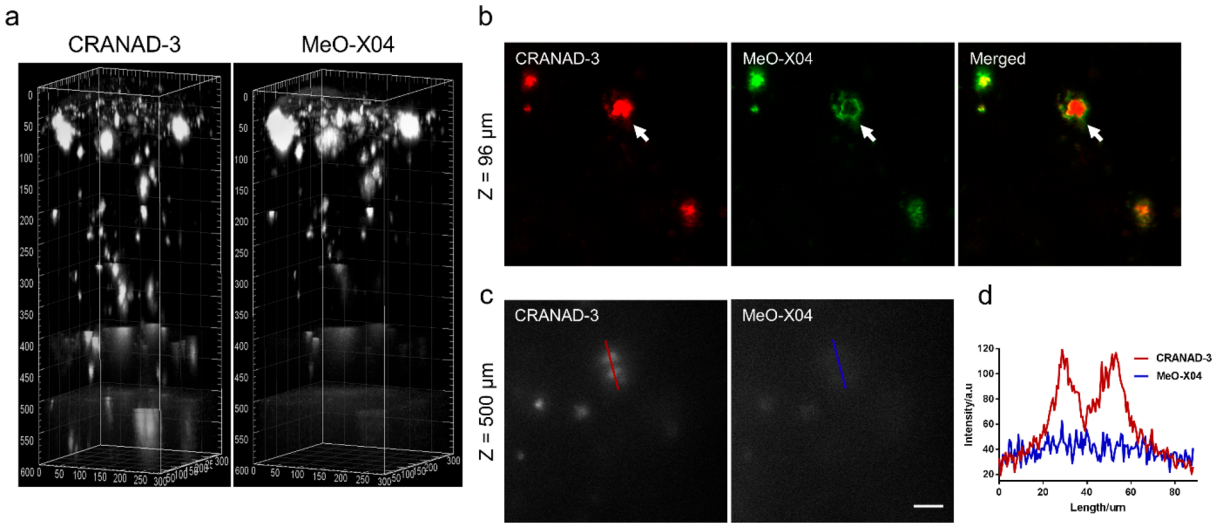

Figure 3. Imaging depth comparison of CRANAD-3 and MeO-X04. (a) Deep brain imaging of amyloid plaques in a 17-month-old APP/PS1 mouse coinjected with CRANAD-3 (4 mg/kg) and MeO-X04 (5 mg/kg). The *z*-step in the stack is 2 μm. The 3D image was reconstructed based on the *z*-stack TPEF images using the commercial *Imaris* software. (b) TPEF images at upper layer (96 μm depth) in (a), showing differences in plaque labeling of CRANAD-3 and MeO-X04, a dense-core plaque is indicted by the white arrow. (c) TPEF images at deeper region (500 μm depth) and (d) quantitative comparison of SBR of amyloid plaques in (c). Scale bar: 40 μm.

the out-of-focus fluorescence in the brain surface,[46] the CRANAD-3 image can still clearly resolve the detailed structure of amyloid plaques with 4.1 peak SBR (Figure 3d). In our study, the largest imaging depth where amyloid plaques were still detectable (SBR ~ 1.0) was about 900 μm. Although we observed photobleaching of CRANAD-3 under two-photon excitation, this only became significant when a high excitation power was applied to the superficial amyloid plaques (>80 mW). At low excitation power (<10 mW) or for deep-tissue imaging (>500 μm, 120 mW), the photobleaching effect was not obvious. Based on the results, we conclude that TPEF imaging with CRANAD-3 probe provides much deeper penetration than the commonly used MeO-X04 and CRANAD-3 is more suitable for two-photon deep brain imaging of amyloid plaques. It should be noted that although the images in Figure 3a show more plagues in superficial layer than deeper layers, we observed the opposite distribution of plagues in other mice. Based on the results from all the AD mice (APP/PS1) used in our study, we found that the distribution of amyloid plaques is highly heterogeneous in cortex, which varies from individual mouse to individual mouse.

Microglial Responses to CRANAD-3 Probe. Microglia are the brain-resident phagocytes, and their roles in neuroinflammation are critical in pathogenesis of AD.[47] The resting microglia behave dynamically by using their motile processes to detect any changes in brain homeostasis, and can transform into less ramified or amoeboid phenotypes with phagocytic capability upon acute or chronic activation of different stimuli.[48] For studying the interaction of microglia and amyloid plaques in vivo that involves the plaque labeling with a fluorescent dye probe, whether the foreign dye causes microglial activation must be addressed beforehand. In this study, we used CX3CR1-EYFP and APP/PS1 × CX3CR1-EYFP mice to investigate whether CRANAD-3 at imaging dose might trigger microglial immune responses in both normal and AD brain, respectively.

To visualize the microglia activities in TPEF image clearly, we first applied the spectral unmixing method to remove lipofuscin interferences in both circumstances. Here, the TPEF signals of EYFP, lipofuscin and CRANAD-3 were collected by two channels (green, 525 ± 25 nm; red, 620 ± 30 nm) at 920 nm excitation. The representative TPEF images are shown in Figure 4. For CX3CR1-EYFP mice with microglia labeled by EYFP, the microglial processes and protrusions are significantly contaminated by the widely distributed lipofuscin granules (<2 μm in diameter) as shown in the upper panel of Figure 4a. After applying spectral unmixing, the spectral ratio helps to identify that a number of lipofuscins (colored in magenta in Figure 4b) colocalize in the microglial soma even though the majority are in its extracellular space, suggesting that microglia is one possible source of lipofuscin. The image of microglia after removal of lipofuscin using the spectral unmixing method is displayed in Figure 4c.

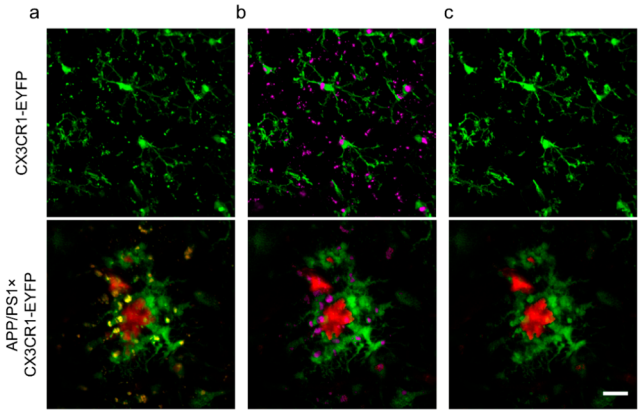

Figure 4. Lipofuscin removal using spectral unmixing in CX3CR1-EYFP (upper row) and APP/PS1 × CX3CR1-EYFP (bottom row) mice. (a) Raw images before lipofuscin removal. Upper panel, single-channel (525 ± 25 nm) image; lower panel, merged image of two channels (green, 525 ± 25 nm; red, 620 ± 30 nm). (b) Differentiation of lipofuscin (magenta) from EYFP (green) and CRANAD-3 (red). (c) After lipofuscin removal. Scale bar: 20 μm

DOI: 10.1021/acschemneuro.8b00306
ACS Chem. Neurosci. 2018, 9, 3128−3136

For APP/PS1 × CX3CR1-EYFP mice, removal of lipofuscin interference was especially necessary for investigating the phagocytic activity of microglia with the presence of amyloid plaques, because the phagocytic products in microglia are morphologically similar to lipofuscin.[49] The ratio-based spectral unmixing method is also applicable for lipofuscin removal from both EYFP and CRANAD-3 images, as can be seen in the bottom row of Figure 4. In detail, since the broad spectrum of lipofuscin covers both EYFP and CRANAD-3, the spectral ratio of these two channels (green, 525 ± 25 nm; red, 620 ± 30 nm) is distinct for lipofuscin, EYFP, and CRANAD-3 and thus can be used to differentiate these three components, as shown in Figure 4b. After spectral unmixing, we could then obtain lipofuscin-free image of EYFP labeled microglia and CRANAD-3 labeled amyloid plaques (Figure 4c). In the following experiments to study the effect of CRANAD-3 on microglia, we have applied the unmixing methods to remove lipofuscin from all TPEF images.

Next, we conducted time-lapse in vivo imaging in CX3CR1-EYFP and APP/PS1 × CX3CR1-EYFP mice to evaluate the effect of CRANAD-3 on microglial activities. We used thinned-skull window, a minimally invasive procedure, for the following experiments. The thinned-skull window procedure is less likely to cause brain injury and induce extensive microglial activation which will surely occur in the case of open-skull window.[50] The representative images of CX3CR1-EYFP mice are shown in Figure 5. As shown in Figure 5a and b, microglial somata

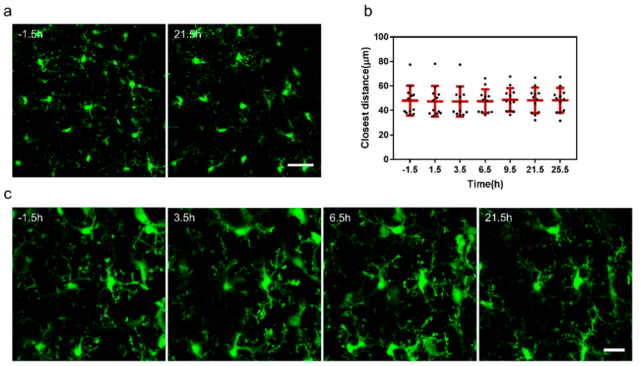

Figure 5. Time-lapse in vivo imaging of microglial activity after CRANAD-3 injection (2 mg/kg) in the CX3CR1-EYFP mice. (a) Microglial density is stable throughout the period indicated by (b) the closest distance between each soma and its neighbors at different time points. (c) Microglia did not show obvious sign of activation as inferred from its ramified morphology. CRANAD-3 was injected at 0 h; the images of −1.5 h was captured 20 h after thinned-skull preparation. Scale bar: 40 μm in (a) and 20 μm in (c).

remained stationary throughout the imaging sessions, and the distance between each soma and its nearest neighbor was barely changed, indicating that its homogeneous distribution was unperturbed. Furthermore, the fine processes of ramified microglia were persisted for over 20 h after CRANAD-3 injection without undergoing significant extension or retraction, as shown in Figure 5c. Together, these results show that resting microglia in the healthy mice brain is not activated by CRANAD-3 administration at the TPEF imaging dosage.

In AD mice brain, microglia adopt a primed phenotype with plaque-dependent heterogeneous distribution, and can be more vulnerable to the inflammatory stimulus than in normal brain.[51,52] To investigate whether CRANAD-3 will alter microglial stability surrounding the plaques, we imaged the microglial dynamics in the APP/PS1 × CX3CR1-EYFP mice for over 26 h following CRANAD-3 administration. Specifically, the dosage of injected CRANAD-3 was selected at 2 mg/kg to make the signal levels of both CRANAD-3 and EYFP similar at 920 nm excitation. The imaging session started at 1.5 h after dye injection when the plaque had been well stained. A stability index defined by the percentage of immobile microglia near plaque region was used to evaluate microglial stability around the amyloid plaques. Figure 6 shows that nearly all

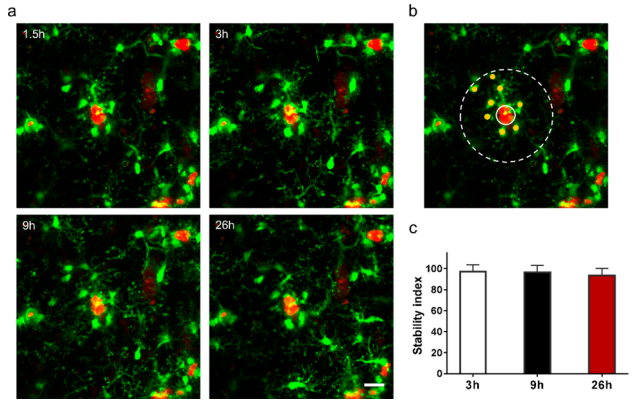

Figure 6. Time-lapse in vivo imaging of microglial activity after CRANAD-3 injection (2 mg/kg) in the APP/PS1 × CX3CR1-EYFP mice. (a) Representatives images showing microglia remain stable surrounding amyloid plaques. (b) Quantitative analysis of microglial stability near plaque region; microglia (highlighted in yellow) in the circular region (dotted circle) with 5-fold diameter of the center amyloid plaque (solid circle) are used for calculation; stability index is calculated as the percentage of immobile microglia from 1.5 h to current imaging sessions. (c) Stability index at different time points. Scale bar: 20 μm.

microglia adjacent to an amyloid plaque were stationary throughout the period (mean percentage of 93% ± 0.06; 106 total cells; n = 11 plaques), consistent with the control experiment of a previous study.[53] These results lead to the conclusion that CRANAD-3 at the imaging dosage (2 mg/kg) does not induce microglial inflammatory responses in AD mice brain.

CONCLUSION

In this study, we introduced a NIR probe of Aβ protein, CRANAD-3, for in vivo two-photon deep brain imaging of amyloid plaques in AD mice model. Compared with the commonly used probe MeO-X04, CRANAD-3 has long wavelengths of excitation and emission with peaks at 900 and 650 nm, respectively. This greatly facilitates the imaging capability of amyloid plaques in deep cortical layers through an open skull window owing to the reduced absorption and scattering of brain tissue. We found that the autofluorescence of "aging pigment" lipofuscin could cause severe interference in TPEF imaging of amyloid plaques labeled by CRANAD-3 and other cells/structures labeled by fluorescence proteins. By using the spectroscopic imaging method, we characterized the autofluorecence of lipofuscin in live mice brains, which shows a broad emission spectrum of over 200 nm bandwidth and a typical short lifetime of about 0.4 ns. This unique fluorescence properties of lipofuscin enable us to remove its interference by using a simple ratio-based spectral or lifetime unmixing

DOI: 10.1021/acschemneuro.8b00306
ACS Chem. Neurosci. 2018, 9, 3128−3136

method. This method has been successfully demonstrated in different circumstances including EYFP-labeled microglia and CRANAD-3 labeled amyloid plaques. Finally, we evaluated the microglial immune response to CRANAD-3 injection at the imaging dosage in both CX3CR1-EYFP and APP/PS1 × CX3CR1-EYFP mice using time-lapse two-photon imaging through the thinned skull window, and the results show that CRANAD-3 at an imaging dosage will not lead to obvious microglial inflammation in both normal and AD mice brain. Although the currently studied CRANAD-3 probe with relatively low excitation efficiency may not have optimized design for the applications under two-photon excitation, it serves as a good example for further work on improving the two-photon performances of NIR Aβ probes.

METHODS

TPEF Spectroscopic Imaging System. All spectroscopic imaging experiments in this study were performed with a home-built upright TPEF imaging system. Its schematic is shown in Figure 7. Briefly, the excitation beam was delivered by a tunable mode-locked Ti:sapphire laser (Chameleon, Ultra II, Coherent) with a pulse width below 140 fs and repetition rate of 80 MHz. The laser beam was subsequently collimated with a variable beam expander (BE052-B, Thorlabs) tuned at 0.5× zoom to achieve the optimal beam diameter. The scan engine was based on a dual-axis galvanometric scan head with 3 mm scan mirrors (6210H, Cambridge Technology) and the line scan rate of its fast axis was set to 250 Hz during image acquisitions. After passing through a relay system consisting of a telecentric scan lens (LSM03-BB, Thorlabs) and an infinity-corrected tube lens (TTL200MP, Thorlabs), the scanning beam was directed to a water-immersion objective lens with a 2 mm working distance (XLPLN25XWMP2, 1.05 NA, Olympus) mounted on a motorized actuator (CONEX-LTA-HL, Newport) for axial sectioning. Backward emission light was collected by the same objective and reflected to the detection system by the interchangeable dichroic mirror, DM1 (either FF757-Di01, Semrock or 665dcxr, Chroma).

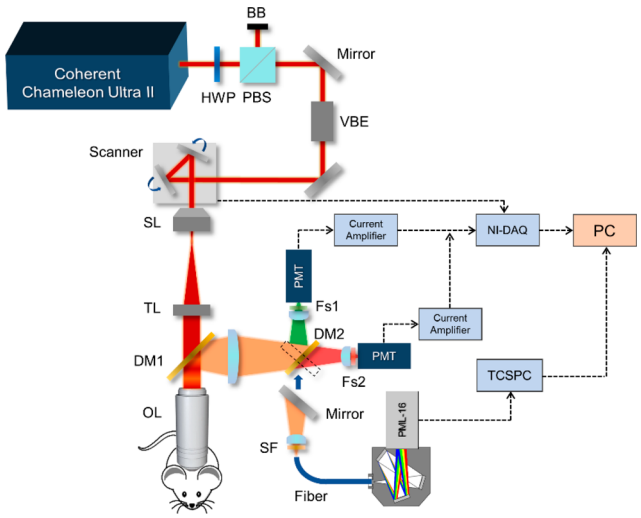

Figure 7. Schematic of two-photon excitation imaging system. HWP, half-wave plate; PBS, polarized beam splitter; BB, beam blocker; VBE, variable beam expander; SL, scan lens; TL, tube lens; DM1,2, dichroic mirror; OL, objective lens; Fs1,2, filter set; SF, short-pass filter; TCSPC, time-correlated single-photon counting; PML-16, 16-channel photomultiplier tube (PMT) for TCSPC.

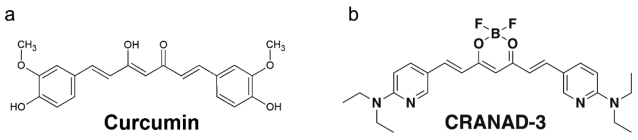

Figure 8. Molecular structures of (a) curcumin and (b) CRANAD-3.

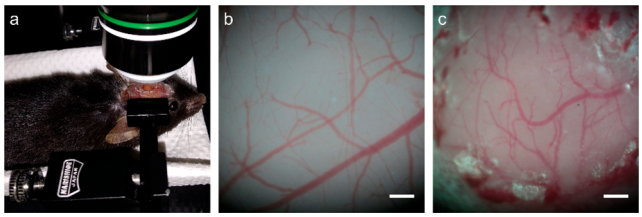

Figure 9. (a) Mouse mounted on an adjustable stage for imaging. (b) Bright-field image through the open-skull window. Scale bar: 0.2 mm. (c) Bright-field image through the thinned-skull window. Scale bar: 0.2 mm.

For emission spectra characterization and lifetime measurement, the collected TPEF signals were reflected from a mirror and coupled into a fiber bundle that directed the signals to a multispectral lifetime detection system. It consists of a spectrograph equipped with a 16-channel photomultiplier tube (PMT) module and a time-correlated single photon counting (TCSPC) module (SPC-150, Becker and Hickl). This detection system is capable of providing both spectral- and time-resolved measurements at each pixel of the TPEF image with a 13 nm spectral resolution and about 150 ps temporal resolution. For CRANAD-3 or lipofuscin characterization, the dichroic mirror DM1 (FF757-Di01, Semrock) reflected fluorescence signal to the detection system while residual excitation laser beam was rejected by a short-pass filter (SF) placed in front of fiber bundle (FF01-770/SP-25, Semrock). The detection system covers a spectral range from 553 to 748 nm by using a spectrograph (ranging from 553 to 748 nm) and a multialkali PMT array (PML-16-C-1, Becker & Hickl) with spectral response from 300 to 820 nm. For MeO-X04 characterization, the dichroic mirror (DM1) and short-pass filter (SF) were switched to 665dcxr and FF01−680/SP-25, respectively. The spectrograph was tuned to the range from 405 to 600 nm and a bialkali PMT array (PML-16-C-0, Becker & Hickl) with spectral response from 300 to 600 nm were used for TPEF detection.

For excitation spectral characterization and deep tissue imaging, the reflective mirror was removed and replaced by another dichroic mirror DM2 (T560lpxr, Chroma). The detection system of spectrograph and multichannel TCSPC module were replaced by a pair of current PMTs (H11461-03 and H10770PA-40, Hamamatsu). The wavelength bands of the signals recorded by the PMTs were determined by the combination of dichroic mirror (DM2) and filter sets (Fs1,2) placed in front of the PMTs. The corresponding PMT signal output was fed into a current amplifier (SR570, Stanford Research and C12419, Hamamatsu, respectively) and then into a multifunction data acquisition (DAQ) device with a 2 M/s sampling rate (PCIe-6361, National Instruments) run by custom-written C# control software. The DAQ board and software also outputted the control signals of the scanner and actuator to form the TPEF images in mouse brain at different depths.

Mice. Mice lines APP/PS1 and CX3CR1-EYFP were purchased from Jackson Laboratory (stock no: 34829-JAX and 021160, respectively). Briefly, the double transgenic APP/PS1 mouse line expresses human APP with Swedish mutation (APPswe) and PSEN1 with exon-9-deleted mutation (PSEN1/dE9) resulting in abundant production of amyloid plaques in the cerebral cortex and hippocampus.[54] The CX3CR1-EYFP mouse line has EYFP expression in microglia because of the knockin of EYFP to the CX3CR1 locus.[55] The APP/PS1 × CX3CR1-EYFP mice were generated by cross-breeding APP/PS1 mice with CX3CR1-EYFP mice. All mice were housed in the Animal and Plant Care Facility of HKUST and 13−17-month old mice were used in this study. All animal procedures were in accordance with an animal protocol approved by the HKUST Animal Ethics Committee.

DOI: 10.1021/acschemneuro.8b00306
ACS Chem. Neurosci. 2018, 9, 3128−3136

Open-Skull Window. Before the surgery, dexamethasone (0.2 μg/mg) solution was subcutaneously administered to prevent brain swelling and reduce inflammatory response. The mouse was then secured on a stereotaxic instrument (model 940, KOPF) and anesthetized by isoflurane during the cranial window implantation, which was slightly modified from a previous report.[56] Briefly, after the exposed skull was cleaned with ethanol (70%), a high-speed drill (K.1070 rotary micromotor kit, Foredem) with a 0.5 mm carbon steel burr (19007-05, Fine Science Tools) was used to perform the 3 mm diameter craniotomy with center at 2 mm lateral and posterior to the bregma point. A compressed sponge (Gelfoam, Pfizer) soaked in saline was applied to the dura matter to stop any bleeding after the craniotomy. Then a sterilized 5 mm round cover glass (150 μm thickness, Warner Instruments) was gently placed on the exposed intact dura and sealed onto the skull by applying a small amount of silicone adhesive (Kwik-Sil, World Precision Instruments) surrounding its edge. After a thin layer of adhesive luting cement (C&B metabond, Parkell Inc.) applied to the skull became dried and hard, a small amount of dental acrylic was used to cover the whole skull surface and also the edge of the cover glass. A custom-designed rectangular head plate with a round hole at the center was then permanently glued to the skull for head fixation during the imaging experiments.

Thinned-Skull Window. The mouse was mounted on the stereotaxic instrument and under isoflurane anesthesia during the surgery, which is based on a previous protocol.[57] Briefly, after the connective tissue on the skull was gently removed by a scalpel, a 0.7 mm carbon steel burr (19007-07, Fine Science Tools) attached to the high-speed drill was used to thin a circular region (1.0−1.5 mm diameter) that centered at 3 mm posterior and 2 mm lateral to the bregma point. Care should be taken during skull thinning and the drill should be moved parallel to instead of against the skull surface. When the outer cortical bone layer and most of the middle cancellous bone were removed, the skull was further manually thinned by using a micro surgical blade (cat. no. 6961, Surgistar) until the skull thickness reached about 40−50 μm, which can be accurately measured by TPEM owing to the second-harmonic generation of bone collagen. A small amount of Metabond cement was used to cover the exposed skull surface surrounding the thinned-skull region, and the custom-designed head plate was then positioned over the center of the window. After the head plate was secured in place, more Metabond cement was applied to the perimeter of the hole in the head plate to create a well for the water-immersion objective used in two-photon imaging. Finally, the exposed thinned-skull window was protected by the biocompatible sealant (Kwik-Cast, World Precision Instruments) which can be peeled off before the imaging experiments.

Reagents and Imaging. The MeO-X04 was obtained from Tocris Bioscience (cat. no. 4920), and the CRANAD-3 was developed and synthesized by Chongzhao Ran's laboratory at Massachusetts General Hospital and Harvard Medical School.[44] Briefly, the design of CRANAD-3 is based on a yellow pigment curcumin which can specifically bind to Aβ deposits owing to its hydrophobic structure,[58] as shown in Figure 8. The red-shifted spectrum of CRANAD-3 is achieved by incorporating a difluoroboronate moiety into the curcumin scaffold. Besides, its capability of Aβ binding is largely enhanced by replacing the phenyl rings with pyridyls that can form hydrogen bond with the Aβ peptide. When the probe becomes conformationally restricted upon Aβ binding, its fluorescence properties will change correspondingly such as increases in quantum yield and blue shift of emission spectrum.[44] This can provide a great contrast for amyloid plaque imaging. For dye preparation and injection, MeO-X04 was intraperitoneally (i.p.) injected (5.0 mg/kg, 10% DMSO, 90% PBS) 4 h prior to imaging, and CRANAD-3 was intravenously (i.v.) delivered by tail-vein injection (2.0−4.0 mg/kg, 15% DMSO, 15% cremophor, 70% PBS) 1.5 h before in vivo imaging of amyloid plaques. The major reason for the different time delay of injection between MeO-X04 and CRANAD-3 is due to their different delivery routes following the injection protocols.[44,59] It normally takes longer time for i.p. injection to deliver dye to the brain than that of i.v. injection. During the imaging experiment, the mouse was under ketamine/xylazine anesthesia (10 μL/g) and secured on a head-holding device with an angle adjuster (MAG-2, NARISHIGE, Japan), as shown in Figure 9.

AUTHOR INFORMATION

Corresponding Authors

*E:mail: boip@ust.hk (N.Y.I).
*E-mail: eequ@ust.hk (J.Y.Q.).

ORCID

Congping Chen: 0000-0001-9186-4346
Xuesong Li: 0000-0002-1795-4885
Nancy Y. Ip: 0000-0002-2763-8907

Author Contributions

J.Y.Q. and N.Y.I. conceived of the research idea. C.C. designed and conducted the experiments under the supervision of J.Y.Q. Z.L., B.Z., and C.L. carried out the surgery and dye injection. C.C. and X.L. built the two-photon imaging system and wrote the software. C.C. took the lead in writing the manuscript with input from all other authors.

Funding

This work was supported by the Hong Kong Research Grants Council through Grants 662513, 16103215, 16148816, 16102518, 768113M, 17127015, T13-607/12R, C6002-17G, AOE/M-09/12, and AOE/M-604/16 and Hong Kong University of Science & Technology (HKUST) through Grant RPC10EG33.

Notes

The authors declare no competing financial interest.

ACKNOWLEDGMENTS

CRANAD-3 was a kind gift from Prof. Chongzhao Ran's laboratory at Massachusetts General Hospital and Harvard Medical School.

REFERENCES

(1) Alzheimer's Association (2017) 2017 Alzheimer's disease facts and figures. *Alzheimer's Dementia 13*, 325−373.
(2) Ashe, K. H., and Zahs, K. R. (2010) Probing the biology of Alzheimer's disease in mice. *Neuron 66*, 631−645.
(3) Mattson, M. P. (2004) Pathways towards and away from Alzheimer's disease. *Nature 430*, 631−639.
(4) Markesbery, W. R. (1997) Oxidative Stress Hypothesis in Alzheimer's Disease. *Free Radical Biol. Med. 23*, 134−147.
(5) Francis, P. T., Palmer, A. M., Snape, M., and Wilcock, G. K. (1999) The cholinergic hypothesis of Alzheimer's disease: a review of progress. *J. Neurol., Neurosurg. Psychiatry 66*, 137−147.
(6) Hardy, J. (2006) Alzheimer's disease: The amyloid cascade hypothesis: An update and reappraisal. *J. Alzheimer's Dis. 9*, 151−153.
(7) Small, S. A., and Duff, K. (2008) Linking Aβ and Tau in Late-Onset Alzheimer's Disease: A Dual Pathway Hypothesis. *Neuron 60*, 534−542.
(8) Maccioni, R. B., Farías, G., Morales, I., and Navarrete, L. (2010) The Revitalized Tau Hypothesis on Alzheimer's Disease. *Arch. Med. Res. 41*, 226−231.
(9) Karran, E., Mercken, M., and De Strooper, B. (2011) The amyloid cascade hypothesis for Alzheimer's disease: an appraisal for the development of therapeutics. *Nat. Rev. Drug Discovery 10*, 698−712.
(10) Kumar, A., Singh, A., and Ekavali (2015) A review on Alzheimer's disease pathophysiology and its management: an update. *Pharmacol. Rep. 67*, 195−203.
(11) Rowe, C. C., Ackerman, U., Browne, W., Mulligan, R., Pike, K. L., O'Keefe, G., Tochon-Danguy, H., Chan, G., Berlangieri, S. U., Jones, G., Dickinson-Rowe, K. L., Kung, H. P., Zhang, W., Kung, M.

DOI: 10.1021/acschemneuro.8b00306
ACS Chem. Neurosci. 2018, 9, 3128−3136

P., Skovronsky, D., Dyrks, T., Holl, G., Krause, S., Friebe, M., Lehman, L., Lindemann, S., Dinkelborg, L. M., Masters, C. L., and Villemagne, V. L. (2008) Imaging of amyloid β in Alzheimer's disease with 18F-BAY94−9172, a novel PET tracer: proof of mechanism. *Lancet Neurol. 7*, 129−135.

(12) Cohen, A. D., Rabinovici, G. D., Mathis, C. A., Jagust, W. J., Klunk, W. E., and Ikonomovic, M. D. (2012) Using Pittsburgh Compound B for In Vivo PET Imaging of Fibrillar Amyloid-Beta. *Adv. Pharmacol. 64*, 27−81.

(13) Kogure, D., Matsuda, H., Ohnishi, T., Asada, T., Uno, M., Kunihiro, T., Nakano, S., and Takasaki, M. (2000) Longitudinal evaluation of early Alzheimer's disease using brain perfusion SPECT. *J. Nucl. Med. 41*, 1155−1162.

(14) Hirao, K., Ohnishi, T., Hirata, Y., Yamashita, F., Mori, T., Moriguchi, Y., Matsuda, H., Nemoto, K., Imabayashi, E., Yamada, M., Iwamoto, T., Arima, K., and Asada, T. (2005) The prediction of rapid conversion to Alzheimer's disease in mild cognitive impairment using regional cerebral blood flow SPECT. *NeuroImage 28*, 1014−1021.

(15) Greicius, M. D., Srivastava, G., Reiss, A. L., and Menon, V. (2004) Default-mode network activity distinguishes Alzheimer's disease from healthy aging: Evidence from functional MRI. *Proc. Natl. Acad. Sci. U. S. A. 101*, 4637−4642.

(16) Higuchi, M., Iwata, N., Matsuba, Y., Sato, K., Sasamoto, K., and Saido, T. C. (2005) ^{19}F and ^{1}H MRI detection of amyloid β plaques *in vivo*. *Nat. Neurosci. 8*, 527−533.

(17) Ran, C., Xu, X., Raymond, S. B., Ferrara, B. J., Neal, K., Bacskai, B. J., Medarova, Z., and Moore, A. (2009) Design, Synthesis, and Testing of Difluoroboron-Derivatized Curcumins as Near-Infrared Probes for in Vivo Detection of Amyloid-β Deposits. *J. Am. Chem. Soc. 131*, 15257−15261.

(18) Hintersteiner, M., Enz, A., Frey, P., Jaton, A.-L., Kinzy, W., Kneuer, R., Neumann, U., Rudin, M., Staufenbiel, M., Stoeckli, M., Wiederhold, K.-H., and Gremlich, H.-U. (2005) In vivo detection of amyloid-β deposits by near-infrared imaging using an oxazine-derivative probe. *Nat. Biotechnol. 23*, 577.

(19) Stone, N., Kerssens, M., Lloyd, G. R., Faulds, K., Graham, D., and Matousek, P. (2011) Surface enhanced spatially offset Raman spectroscopic (SESORS) imaging − the next dimension. *Chemical Science 2*, 776.

(20) Liao, C. R., Rak, M., Lund, J., Unger, M., Platt, E., Albensi, B. C., Hirschmugl, C. J., and Gough, K. M. (2013) Synchrotron FTIR reveals lipid around and within amyloid plaques in transgenic mice and Alzheimer's disease brain. *Analyst 138*, 3991.

(21) Klunk, W. E., Bacskai, B. J., Mathis, C. A., Kajdasz, S. T., McLellan, M. E., Frosch, M. P., Debnath, M. L., Holt, D. P., Wang, Y., and Hyman, B. T. (2002) Imaging Abeta plaques in living transgenic mice with multiphoton microscopy and methoxy-X04, a systemically administered Congo red derivative. *J. Neuropathol. Exp. Neurol. 61*, 797−805.

(22) Spires, T. L., Meyer-Luehmann, M., Stern, E. A., McLean, P. J., Skoch, J., Nguyen, P. T., Bacskai, B. J., and Hyman, B. T. (2005) Dendritic Spine Abnormalities in Amyloid Precursor Protein Transgenic Mice Demonstrated by Gene Transfer and Intravital Multiphoton Microscopy. *J. Neurosci. 25*, 7278−7287.

(23) Paraskevaidi, M., Morais, C. L. M., Lima, K. M. G., Snowden, J. S., Saxon, J. A., Richardson, A. M. T., Jones, M., Mann, D. M. A., Allsop, D., Martin-Hirsch, P. L., and Martin, F. L. (2017) Differential diagnosis of Alzheimer's disease using spectrochemical analysis of blood. *Proc. Natl. Acad. Sci. U. S. A. 114*, E7929−E7938.

(24) Denk, W., Strickler, J. H., and Webb, W. W. (1990) Two-photon laser scanning fluorescence microscopy. *Science 248*, 73−76.

(25) Helmchen, F., and Denk, W. (2005) Deep tissue two-photon microscopy. *Nat. Methods 2*, 932.

(26) Christie, R. H., Bacskai, B. J., Zipfel, W. R., Williams, R. M., Kajdasz, S. T., Webb, W. W., and Hyman, B. T. (2001) Growth Arrest of Individual Senile Plaques in a Model of Alzheimer's Disease Observed by In Vivo Multiphoton Microscopy. *J. Neurosci. 21*, 858−864.

(27) Hefendehl, J. K., Wegenast-Braun, B. M., Liebig, C., Eicke, D., Milford, D., Calhoun, M. E., Kohsaka, S., Eichner, M., and Jucker, M. (2011) Long-term in vivo imaging of β-amyloid plaque appearance and growth in a mouse model of cerebral β-amyloidosis. *J. Neurosci. 31*, 624−629.

(28) Bolmont, T., Haiss, F., Eicke, D., Radde, R., Mathis, C. A., Klunk, W. E., Kohsaka, S., Jucker, M., and Calhoun, M. E. (2008) Dynamics of the Microglial/Amyloid Interaction Indicate a Role in Plaque Maintenance. *J. Neurosci. 28*, 4283−4292.

(29) Dong, J., Revilla-Sanchez, R., Moss, S., and Haydon, P. G. (2010) Multiphoton in vivo imaging of amyloid in animal models of Alzheimer's disease. *Neuropharmacology 59*, 268−275.

(30) Burgold, S., Bittner, T., Dorostkar, M. M., Kieser, D., Fuhrmann, M., Mitteregger, G., Kretzschmar, H., Schmidt, B., and Herms, J. (2011) In vivo multiphoton imaging reveals gradual growth of newborn amyloid plaques over weeks. *Acta Neuropathol. 121*, 327−335.

(31) Horton, N. G., Wang, K., Kobat, D., Clark, C. G., Wise, F. W., Schaffer, C. B., and Xu, C. (2013) In vivo three-photon microscopy of subcortical structures within an intact mouse brain. *Nat. Photonics 7*, 205.

(32) Tong, H., Lou, K., and Wang, W. (2015) Near-infrared fluorescent probes for imaging of amyloid plaques in Alzheimer's disease. *Acta Pharm. Sin. B 5*, 25−33.

(33) Xu, M., Ren, W., Tang, X., Hu, Y., and Zhang, H. (2016) Advances in development of fluorescent probes for detecting amyloid-β aggregates. *Acta Pharmacol. Sin. 37*, 719.

(34) Gray, D. A., and Woulfe, J. (2005) Lipofuscin and Aging: A Matter of Toxic Waste. *Sci. Aging Knowl. Environ. 2005*, re1.

(35) Rota, M., Goichberg, P., Anversa, P., and Leri, A. (2011) Aging Effects on Cardiac Progenitor Cell Physiology. In *Comprehensive Physiology*, John Wiley & Sons, Inc.

(36) Zipfel, W. R., Williams, R. M., Christie, R., Nikitin, A. Y., Hyman, B. T., and Webb, W. W. (2003) Live tissue intrinsic emission microscopy using multiphoton-excited native fluorescence and second harmonic generation. *Proc. Natl. Acad. Sci. U. S. A. 100*, 7075−7080.

(37) Kwan, A. C., Duff, K., Gouras, G. K., and Webb, W. W. (2009) Optical visualization of Alzheimer's pathology via multiphoton-excited intrinsic fluorescence and second harmonic generation. *Opt. Express 17*, 3679−3689.

(38) Eichhoff, G., Busche, M. A., and Garaschuk, O. (2008) In vivo calcium imaging of the aging and diseased brain. *Eur. J. Nucl. Med. Mol. Imaging 35*, 99−106.

(39) Drobizhev, M., Makarov, N. S., Tillo, S. E., Hughes, T. E., and Rebane, A. (2011) Two-photon absorption properties of fluorescent proteins. *Nat. Methods 8*, 393−399.

(40) ISS Data Tables, Lifetime Data of Selected Fluorophores.

(41) Heo, C. H., Kim, K. H., Kim, H. J., Baik, S. H., Song, H., Kim, Y. S., Lee, J., Mook-jung, I., and Kim, H. M. (2013) A two-photon fluorescent probe for amyloid-β plaques in living mice. *Chem. Commun. (Cambridge, U. K.) 49*, 1303−1305.

(42) Ran, C., and Moore, A. (2012) Spectral unmixing imaging of wavelength-responsive fluorescent probes: an application for the real-time report of amyloid Beta species in Alzheimer's disease. *Mol. Imaging Biol. 14*, 293−300.

(43) Zhang, X., Tian, Y., Yuan, P., Li, Y., Yaseen, M. A., Grutzendler, J., Moore, A., and Ran, C. (2014) A bifunctional curcumin analogue for two-photon imaging and inhibiting crosslinking of amyloid beta in Alzheimer's disease. *Chem. Commun. 50*, 11550−11553.

(44) Zhang, X., Tian, Y., Zhang, C., Tian, X., Ross, A. W., Moir, R. D., Sun, H., Tanzi, R. E., Moore, A., and Ran, C. (2015) Near-infrared fluorescence molecular imaging of amyloid beta species and monitoring therapy in animal models of Alzheimer's disease. *Proc. Natl. Acad. Sci. U. S. A. 112*, 9734−9739.

(45) Shi, L., Sordillo, L. A., Rodriguez-Contreras, A., and Alfano, R. (2016) Transmission in near-infrared optical windows for deep brain imaging. *Journal of Biophotonics 9*, 38−43.

DOI: 10.1021/acschemneuro.8b00306
ACS Chem. Neurosci. 2018, 9, 3128−3136

(46) Theer, P., and Denk, W. T. (2004) *On the fundamental imaging-depth limit in two-photon microscopy* (Avrillier, S., and Tualle, J.-M., Eds.), p 45.
(47) Heneka, M. T., Carson, M. J., Khoury, J. E., Landreth, G. E., Brosseron, F., Feinstein, D. L., Jacobs, A. H., Wyss-Coray, T., Vitorica, J., Ransohoff, R. M., Herrup, K., Frautschy, S. A., Finsen, B., Brown, G. C., Verkhratsky, A., Yamanaka, K., Koistinaho, J., Latz, E., Halle, A., Petzold, G. C., Town, T., Morgan, D., Shinohara, M. L., Perry, V. H., Holmes, C., Bazan, N. G., Brooks, D. J., Hunot, S., Joseph, B., Deigendesch, N., Garaschuk, O., Boddeke, E., Dinarello, C. A., Breitner, J. C., Cole, G. M., Golenbock, D. T., and Kummer, M. P. (2015) Neuroinflammation in Alzheimer's disease. *Lancet Neurol. 14*, 388−405.
(48) Parkhurst, C. N., and Gan, W.-B. (2010) Microglia dynamics and function in the CNS. *Curr. Opin. Neurobiol. 20*, 595−600.
(49) Nimmerjahn, A., Kirchhoff, F., and Helmchen, F. (2005) Resting Microglial Cells Are Highly Dynamic Surveillants of Brain Parenchyma in Vivo. *Science 308*, 1314−1318.
(50) Xu, H.-T., Pan, F., Yang, G., and Gan, W.-B. (2007) Choice of cranial window type for in vivo imaging affects dendritic spine turnover in the cortex. *Nat. Neurosci. 10*, 549−551.
(51) Perry, V. H., and Holmes, C. (2014) Microglial priming in neurodegenerative disease. *Nat. Rev. Neurol. 10*, 217−224.
(52) Plescher, M., Seifert, G., Hansen, J. N., Bedner, P., Steinhauser, C., and Halle, A. (2018) Plaque-dependent morphological and electrophysiological heterogeneity of microglia in an Alzheimer's disease mouse model. *Glia 66*, 1464.
(53) Liu, Z., Condello, C., Schain, A., Harb, R., and Grutzendler, J. (2010) CX3CR1 in Microglia Regulates Brain Amyloid Deposition through Selective Protofibrillar Amyloid- Phagocytosis. *J. Neurosci. 30*, 17091−17101.
(54) Jankowsky, J. L., Fadale, D. J., Anderson, J., Xu, G. M., Gonzales, V., Jenkins, N. A., Copeland, N. G., Lee, M. K., Younkin, L. H., Wagner, S. L., Younkin, S. G., and Borchelt, D. R. (2004) Mutant presenilins specifically elevate the levels of the 42 residue beta-amyloid peptide in vivo: evidence for augmentation of a 42-specific gamma secretase. *Hum. Mol. Genet. 13*, 159−170.
(55) Parkhurst, C. N., Yang, G., Ninan, I., Savas, J. N., Yates, J. R., Lafaille, J. J., Hempstead, B. L., Littman, D. R., and Gan, W.-B. (2013) Microglia promote learning-dependent synapse formation through brain-derived neurotrophic factor. *Cell 155*, 1596−1609.
(56) Mostany, R., and Portera-Cailliau, C. (2008) A craniotomy surgery procedure for chronic brain imaging. *J. Visualized Exp.*, 680.
(57) Yang, G., Pan, F., Parkhurst, C. N., Grutzendler, J., and Gan, W.-B. (2010) Thinned-skull cranial window technique for long-term imaging of the cortex in live mice. *Nat. Protoc. 5*, 201−208.
(58) Yang, F., Lim, G. P., Begum, A. N., Ubeda, O. J., Simmons, M. R., Ambegaokar, S. S., Chen, P. P., Kayed, R., Glabe, C. G., Frautschy, S. A., and Cole, G. M. (2005) Curcumin Inhibits Formation of Amyloid β Oligomers and Fibrils, Binds Plaques, and Reduces Amyloid in Vivo. *J. Biol. Chem. 280*, 5892−5901.
(59) Fu, A. K. Y., Hung, K.-W., Yuen, M. Y. F., Zhou, X., Mak, D. S. Y., Chan, I. C. W., Cheung, T. H., Zhang, B., Fu, W.-Y., Liew, F. Y., and Ip, N. Y. (2016) IL-33 ameliorates Alzheimer's disease-like pathology and cognitive decline. *Proc. Natl. Acad. Sci. U. S. A. 113*, E2705−E2713.

DOI: 10.1021/acschemneuro.8b00306
ACS Chem. Neurosci. 2018, 9, 3128−3136